Materials Today Energy 48 (2025) 101810

Contents lists available at ScienceDirect

Materials Today Energy

journal homepage: www.journals.elsevier.com/materials-today-energy/

Overcoming instability challenges of binder-free, self-standing 1T-TiS_2 electrodes in aqueous symmetric supercapacitors through dopamine functionalization

Ali Deniz Ucar [a], Sumeyye Kandur Baglicakoglu [a], Mete Batuhan Durukan [a], Murathan Cugunlular [a], Sena Oz [a], Yusuf Kocak [b], Burak Ülgüt [b], Emrah Ozensoy [b,c], Husnu Emrah Unalan [a,d,*]

[a] Department of Metallurgical and Materials Engineering, Middle East Technical University (METU), 06800, Ankara, Türkiye
[b] Department of Chemistry, Bilkent University, 06800, Ankara, Türkiye
[c] UNAM-National Nanotechnology Center, Bilkent University, 06800, Ankara, Türkiye
[d] Energy Storage Materials and Devices Research Center (ENDAM), Middle East Technical University (METU), 06800, Ankara, Türkiye

ARTICLE INFO

Keywords:
Titanium disulfide
Supercapacitors
Dopamine functionalization
Transition metal dichalcogenides

ABSTRACT

Two-dimensional materials draw considerable interest for energy storage. Semimetallic phases of transition metal dichalcogenides (TMDs), notably titanium disulfide (TiS_2), are extensively studied for their distinctive electronic, chemical, and optical traits. TiS_2, initially proposed for Li-ion batteries, holds promise for supercapacitors, although its utilization faces stability challenges in aqueous environments. Herein, electrically conducting and surface-passivated 2D 1T-TiS_2 flakes were fabricated and tailored for application as electrodes in supercapacitors with enhanced durability. For this purpose, self-standing and flexible 1T-TiS_2 films were fabricated using vacuum filtration and treated with dopamine (DA) to obtain electrochemically stable supercapacitor electrodes in aqueous environments. During DA treatment, in-situ generation of hydrogen peroxide (H_2O_2) leads to the formation of a thin titanium dioxide (TiO_2) overlayer on TiS_2, enhancing oxidation stability. At a scan rate of 10 mV s^{-1}, a single electrode demonstrated a gravimetric specific capacitance of 128 F g^{-1}, a volumetric specific capacitance of 122 F cm^{-3}, and an areal specific capacitance of 244 mF cm^{-2}. The symmetric supercapacitor device demonstrated an impressive capacity retention of 96.1 % after 10000 cycles and 85.5 % after 18000 cycles. These results pave the way for utilizing 2D 1T-TiS_2 in aqueous environments, expanding its possible applications and holding promise for significant advancements in the field.

1. Introduction

Supercapacitors, also known as electric double-layer capacitors or ultracapacitors, are energy storage devices with high power and low internal resistance. Compared to batteries, they can store and deliver energy at relatively high rates because their energy storage mechanism only requires a simple charge separation at the electrode and electrolyte interface by adsorption of ions [1,2]. Supercapacitors provide benefits such as long life, high power, flexible packaging, wide range of operation temperatures, low maintenance, and low weight compared to other energy storage technologies [3,4]. Due to their advantageous characteristics, supercapacitors are ideally suited for large-scale applications that need high power and short response times, such as forklifts [5], load cranes [5], grid stabilization systems [5], uninterruptible power supplies [5], hybrid electrical vehicles [5], high-speed transportation [5], regenerative braking [6], and small-scale applications such as wearable electronics [7,8], sensors [9,10], and consumer electronics [11,12].

Layer-structured graphene is one of the most famous two-dimensional (2D) electrode materials for supercapacitors due to its high electrical conductivity, chemical durability, and large specific surface area [3,13]. Expanded layers in self-standing 2D materials

* Corresponding author. Department of Metallurgical and Materials Engineering, Middle East Technical University (METU), 06800, Ankara, Türkiye.
E-mail addresses: alidenizucar33@gmail.com (A.D. Ucar), sumeyyekandur@gmail.com (S.K. Baglicakoglu), bdurukan@metu.edu.tr (M.B. Durukan), murathan.cugunlular@metu.edu.tr (M. Cugunlular), sena.oz@metu.edu.tr (S. Oz), yusuf.kocak@bilkent.edu.tr (Y. Kocak), ulgut@fen.bilkent.edu.tr (B. Ülgüt), ozensoy@fen.bilkent.edu.tr (E. Ozensoy), unalan@metu.edu.tr (H.E. Unalan).

https://doi.org/10.1016/j.mtener.2025.101810
Received 11 October 2024; Received in revised form 31 December 2024; Accepted 14 January 2025
Available online 15 January 2025

facilitate ion transport, improving ion diffusion pathways and enhancing overall electrochemical performance. This structural modification, along with the use of techniques like vacuum filtration to fabricate self-standing electrodes without binders, enhances charge storage efficiency by improving ion accessibility to active sites. Transition metal dichalcogenides (TMDs) constitute another class of layer-structured materials that belong to a category of materials denoted by the formula MX_2, where M represents elements such as molybdenum (Mo), vanadium (V), tungsten (W), or titanium (Ti), while X represents chalcogen elements like sulfur (S), selenium (Se), or tellurium (Te) [14]. The M-X interactions in TMDs are characterized by strong covalent bonding, forming X-M-X layers. Meanwhile, weak van der Waals interactions occur between adjacent MX_2 layers along the *c*-axis, and repeating X-M-X layers form bulk materials [15]. Those weak van der Waals bonds can be broken to obtain single or few-layered 2D TMDs. Depending on the arrangements of their atoms, 1T and 2H phases are commonly observed in 2D TMDs. In the 2H phase, metal atoms are attached to chalcogen atoms, and there is stacking in the form of ABA (X-M-X), while there is stacking in the form of ABC (X-M-X) in the 1T phase. These phases can show semiconductor or semimetallic properties [16]. While TMDs with fully occupied *d*-orbitals show semiconductor properties, TMDs without filled *d*-orbitals show semimetallic properties. The arrangement of atoms within the single layer is intricately influenced by the occupancy state of *d*-orbitals, which is pivotal in determining the phase of TMDs [17]. In the field of materials science, 2D TMDs have garnered significant research attention and have been extensively investigated in recent years [18–21]. Among TMDs, molybdenum disulfide (MoS_2) attracted the most attention due to its durability. Following MoS_2, molybdenum diselenide ($MoSe_2$), tungsten disulfide (WS_2) and tungsten diselenide (WSe_2) are the most investigated materials especially for energy storage and conversion [22,23], electronics [24,25], optoelectronics [24,26], sensing [27,28] and thermoelectric devices [29,30].

Titanium disulfide (TiS_2) is the lightest member of the TMDs [31]. Similar to other TMDs, 2H-TiS_2 exhibits semiconductor behavior, while its stable phase, 1T-TiS_2, demonstrates semimetallic behavior [32–34]. The use of TiS_2 has been demonstrated in nitrogen dioxide (NO_2), hydrogen sulfide (H_2S), oxygen (O_2), deoxyribonucleic acid (DNA), and catechol sensors [35–38], perovskite and dye-sensitized solar cells [39,40], wearable electronics [41], thermoelectric [42] and nonlinear optical limiting applications [43]. Besides serving as the cathode material in the first practical Li-ion battery [44], TiS_2 has found extensive applications as a cathode or additive material in various energy storage devices, including lithium-sulfur [31,45–47], sodium-ion [48–50], lithium-ion [51], potassium-ion [52], and magnesium-ion [53] batteries. Nevertheless, 2D TiS_2 is susceptible to oxidation in water and air, with moisture being the primary catalyst for this process [48,54]. Conversion to titanium dioxide (TiO_2) occurs in such cases, and toxic and corrosive H_2S gas is released as a by-product [55,56].

The application of TiS_2 as a supercapacitor electrode for aqueous environments has been investigated in a limited number of recent studies. Takayanagi et al. [57] developed TiS_2 and graphene oxide heterostructures using a colloidal association method, achieving a specific capacitance of 113 F g^{-1} and a 41 % performance improvement. In this study, reduced graphene oxide (rGO) serves as the primary capacitive material, while TiS_2 enhances its performance by preventing restacking, increasing surface area, and facilitating charge carrier transport. Rahman et al. [58] fabricated symmetric supercapacitors by electrochemically depositing TiS_2, reporting an energy density of 34.35 mWh cm^{-2} and cycling stability with only a 4 % capacitance loss after 5000 cycles. The electrode developed in this study requires a titanium foil substrate, as the TiS_2 thin film is electrochemically synthesized directly on its surface. These studies demonstrate innovative approaches to enhancing the performance of TiS_2 through diverse fabrication methods. However, most rely on binder/conductive additive use and evaluate electrochemical performance in three-electrode systems rather than full device configurations. While Rahman et al. [58] conducted device-level measurements, none of the works explored self-standing 2D TiS_2 electrodes or stability testing beyond 5000 cycles. This highlights a research gap, emphasizing the need for further studies on self-standing 2D TiS_2 electrodes and extended stability assessments to fully realize their potential in practical energy storage applications.

Here, a tailored process was developed to guarantee the long-term stability of 2D TiS_2 in an aqueous environment. These findings are further exemplified through their application as electrode-active materials in symmetric supercapacitors. Subsequent to the bulk TiS_2 production from elemental powders, this work produced self-standing, binder-free, electrically conductive 2D 1T-TiS_2 flakes through organolithium exfoliation. Achieving 2D enables expanded interlayers for easier intercalation on top of excellent electrical conductivity. Moreover, it allows the preparation of self-standing films without the need for a binder. Addressing the stability concerns in aqueous environments, electrodes with enhanced oxidation resistance and electrochemical stability were obtained through dopamine (DA, 2-(3,4-dihydroxyphenyl)ethylamine, $(HO)_2C_6H_3CH_2CH_2NH_2$) treatment, which was found to form a thin layer of TiO_2 by in-situ generated hydrogen peroxide (H_2O_2). This work pioneers the electrochemical stability of TiO_2 passivated 1T-TiS_2 electrodes for symmetric supercapacitors, overcoming stability challenges in aqueous environments and thus offering promising prospects for various other advanced energy storage systems.

2. Results and discussion

The schematic fabrication process of self-standing 1T-TiS_2 film is provided in Fig. S1, Supporting Information. Initially, titanium and sulfur powders are annealed in a vacuum quartz tube, producing bulk TiS_2 powder. The bulk powders are then exfoliated via organolithium exfoliation. Organolithium exfoliation is one of the standard methods for fabricating 2D TMDs [59]. Intercalated Li^+ ions react with water molecules through sonication, producing hydrogen (H_2) gas and lithium hydroxide (LiOH) [60]. As a result of lithium intercalation and the release of H_2 bubbles, the distance between layers increases, leading to a weakening of van der Waals forces [60]. Obtained semimetallic 2D 1T-TiS_2 suspension is vacuum filtered to collect self-standing and binder-free films. Single walled carbon nanotubes (SWCNTs) are added to increase the mechanical stability of the filtered, self-standing TiS_2 films. When DA-treated films are necessary, the treatment is administered prior to the addition of the SWCNTs. Circular electrodes are prepared by punching self-standing films. Detailed information can be found in the experimental section.

Scanning electron microscopy (SEM) images of fabricated bulk and exfoliated TiS_2 are provided in Fig. S2, Supporting Information. As expected, bulk TiS_2 powders collected after annealing in quartz tubes show hexagonal crystal structures (Figs. S2a–b). Following the organolithium exfoliation, we achieved large 2D sheets with lateral dimensions exceeding 30 μm, indicating a successful exfoliation process (Figs. S2c–d). EDAX spectra of bulk and 2D-TiS_2 are given in Figs. S3 (a–b), Supporting Information. An analysis of the atomic percentages of titanium and sulfur atoms confirmed the successful synthesis of bulk TiS_2, and it is evident that exfoliation led to the formation of sulfur vacancies. The presence of defects in the structure leads to a rise in the number of active sites, indicating the potential to modify their surface chemistry and functionality [61]. Through vacuum filtration, binder-free, electrically conducting, self-standing 1T-TiS_2 films are obtained (Fig. 1a). The conductivity of films is measured as 107 ± 7 S cm^{-1} using 4-point probe technique. Compared to SWCNT-free film (Fig. S4, Supporting Information), addition of a small amount of SWCNTs facilitated the formation of self-standing films, showcasing remarkable mechanical flexibility that allowed them to bend without experiencing any structural failure (Fig. 1b). Additionally, it is observed that the addition of SWCNTs increased the conductivity of self-standing 1T-TiS_2 films by

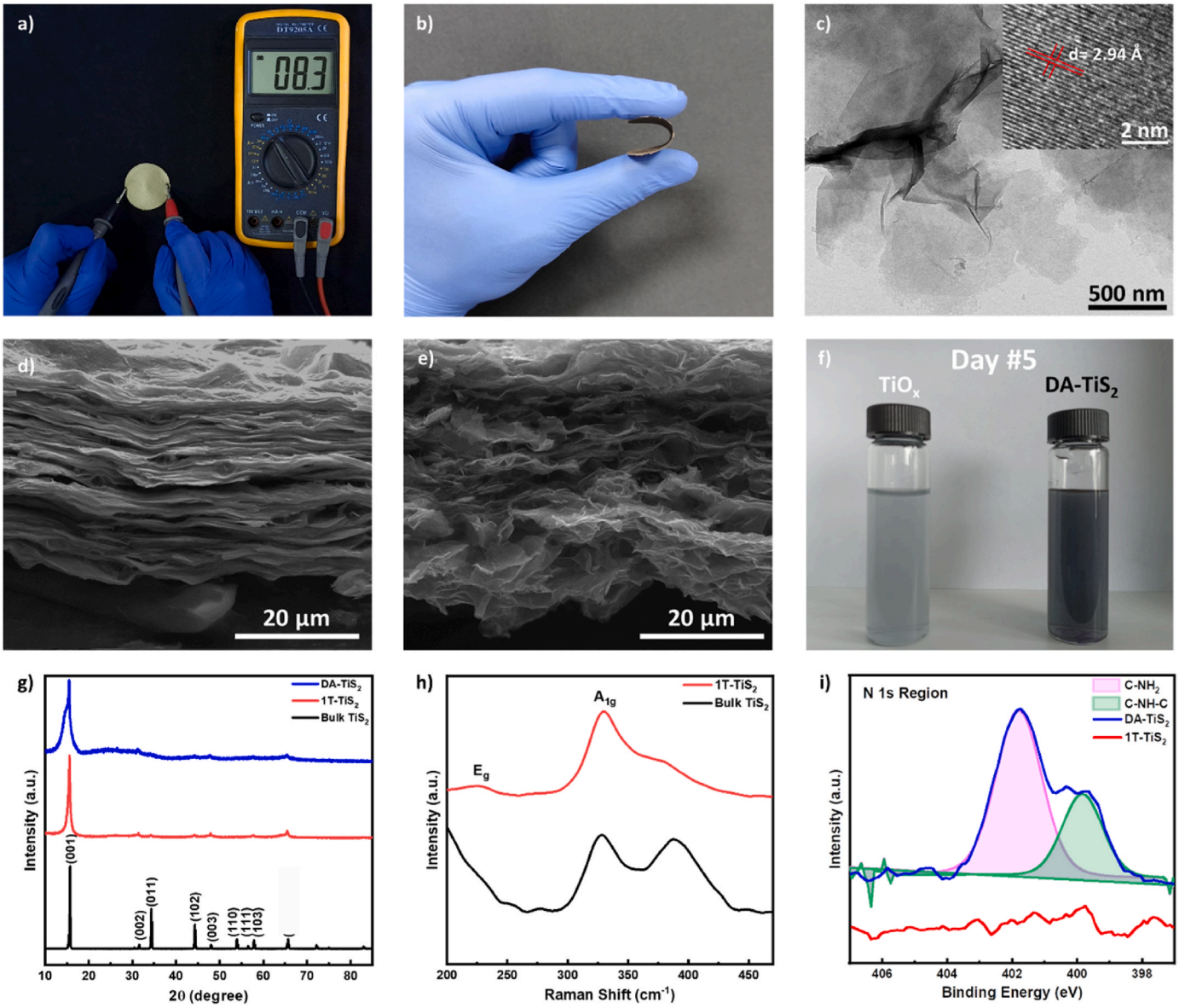

Fig. 1. a) Conductive, self-standing, and b) flexible TiS_2 film. c) HC-TEM images of TiS_2 flakes. Inset shows the HR-TEM image obtained from a single 1T-TiS_2 flake. d) SEM images of DA-free and e) DA-treated TiS_2 films. f) A photo showing the colour difference between as-prepared 2D 1T-TiS_2 and DA-treated TiS_2 dispersions after 5 days. g) XRD patterns of bulk TiS_2 powders, 1T-TiS_2 and DA-treated 1T-TiS_2 (DA-TiS_2) films. h) Raman spectra of bulk TiS_2 and 2D 1T-TiS_2. i) XPS analysis of 1T-TiS_2 and DA-treated TiS_2 films.

66 %, from 107 S cm^{-1}, reaching to 177 S cm^{-1}. With the addition of SWCNTs, a simple bending test is conducted to provide the self-standing films' ability to withstand flexing. The photographs of the setup and the resulting change of resistivity with respect to bending cycles are provided in Fig. S5. Self-standing 1T-TiS_2/SWCNT films are punched to obtain 4.5 cm long strips with circular ends and attached to a custom bending device. The end points are fixed with adhesive tapes onto aluminum foils, which allowed the measurement of the resistance throughout the bending cycles (Fig. S5a). From the initial resistance of 20 Ω, the change in resistance after 2000 bending cycles is found to be only 0.15, indicating the durability of the self-standing films to mild flexing conditions (Fig. S5b). High-resolution (HR-TEM) and high-contrast transmission electron microscopy (HC-TEM) images are provided in Fig. 1c. The calculated lattice spacing of 2.94 Å for the (100) plane aligns well with the literature, providing substantial evidence for the formation of 2D 1T-TiS_2 ($P3m1$ space group) [62,63]. From the HC-TEM image in Fig. 1c, the 2D structure of the TiS_2 is also verified, with the appearance of few-layered nanosheets. Few-layered 1T-TiS_2 structures are then vacuum-filtered to obtain electrically conducting, self-standing films. Cross-sectional SEM images of DA-free and DA-treated films are provided in Fig. 1d–e. The layered structure of 1T-TiS_2 is clearly seen in Fig. 1d. The application of DA resulted in a film with increased volume and a flaky appearance (Fig. 1e).

To show how DA increased the resistance to oxidation in an aqueous environment, as-prepared 2D 1T-TiS_2, and DA-treated 1T-TiS_2 structures are left in distilled water, and the solution color is monitored for 5 days. A photo of the suspensions' initial colors is provided in Fig. S6, Supporting Information. As seen in Fig. 1f, the as-prepared 2D 1T-TiS_2 suspension turned white – indicating the formation of TiO_x. The color of the DA-treated 1T-TiS_2 suspension was still black after 5 days. From here, it was apparent that DA molecules are attached to the TiS_2 flakes, preventing the degradation of their electrochemical functionalities in the aqueous environment. Detrimental extreme oxidation of the as-prepared 1T-TiS_2, which has not been treated with DA, is proven by UV–Vis spectroscopy (Fig. S7, Supporting Information). The absorption spectrum of as-prepared 2D 1T-TiS_2 revealed two primary peaks at

wavelengths of 284 and 632 nm and a smaller peak at 362 nm. After immersion in water for 5 days, the color of the as-prepared 2D 1T-TiS_2 suspension underwent a noticeable change and turned white. Consequently, the absorption spectrum is re-examined. Alongside a reduction in the overall intensity, the peak at a wavelength of 632 nm disappeared. Sherrell et al. [62] elucidated that the reduction in intensity and the disappearance of the peak can be attributed to the agglomeration and formation of TiO_x.

X-ray diffraction (XRD) patterns of as-synthesized bulk TiS_2 powders, as-prepared 1T-TiS_2 film, and DA-treated 1T-TiS_2 film are provided in Fig. 1g. DA-treated 1T-TiS_2 is denoted as DA-TiS_2. The XRD pattern of bulk TiS_2 corresponded to the typical hexagonal pattern of bulk TiS_2 (JCPDS card no. 88–1967). Following organolithium exfoliation, a strong characteristic peak at 15.72° (001) broadened. In contrast, other peaks disappeared due to disrupted crystal structure and increased interplanar distance, providing further evidence for the 2D structure of 1T-TiS_2 and reiterating its few-layered structure. According to Ko et al. [64] the adsorption of ligands onto the surface of 2D nanosheets led to further broadening and formation of a shoulder in XRD pattern. This characteristic shoulder peak is observed due to the adsorption of ligands at (001), which resulted from the DA treatment.

The Raman spectrum of as-exfoliated 2D 1T-TiS_2 nanosheets on silicon wafers revealed three primary peaks located at 225, 331, and 371 (shoulder peak, Sh) cm^{-1} (Fig. 1h). Peaks at 225 and 331 cm^{-1} are identified as two Raman active modes of TiS_2, E_g (in-plane), and A_{1g} (out-of-plane), respectively [62]. It was suggested by Sherrell et al. that the shoulder peak should be more apparent for multi-layered TiS_2 as it was for bulk TiS_2 in Fig. 1h. That shoulder peak was also reported as an indicator of the defective structure of TiS_2 [65,66]. The ratio of peak intensities A_{1g}/Sh is found to be 2, indicating a structure of 2–4 layers [62]. Raman spectroscopy is performed on both the SWCNT-free//TiS_2 film and the SWCNT//TiS_2 film. The analysis revealed no significant or meaningful differences between the two films, indicating that the addition of carbon nanotubes did not result in noticeable changes in the Raman-active vibrational modes of the TiS_2 structure (Fig. S8, Supporting Information). Therefore, Raman characterization further proved the 2D structure of 1T-TiS_2, which is also shown by HC-TEM images in Fig. 1c and XRD analysis in Fig. 1g. In addition, the Raman spectrum of 1T-TiS_2 and DA-TiS_2 vacuum-filtered films obtained following vacuum filtration revealed that DA treatment led to an increase in the anatase phase of TiO_2 on the surface [67] (Fig. S9, Supporting Information). Differences between Raman spectrums of as exfoliated 2D 1T-TiS_2 (Fig. 1h) and vacuum-filtered 1T-TiS_2 and DA-TiS_2 films (Fig. S9, Supporting Information) may be attributed to mechanical restacking of TiS_2 layers during vacuum filtration.

Thorough X-ray photoelectron spectroscopy (XPS) analysis is conducted to comprehend the impact of dopamine (DA) treatment on the TiS_2 structure and establish correlations with the observed enhancement in electrochemical stability, which is discussed later. The results of the XPS analysis are provided in Fig. 1i and Figs. S10–S12, Supporting Information. XPS data of the N1s region of 1T-TiS_2 and DA-TiS_2 films in Fig. 1i revealed the presence of primary (C-NH_2) and secondary amine (C-NH-C) functionalities on DA-TiS_2 at 401.8 and 399.8 eV, respectively, suggesting incomplete polymerization of DA on the surface [68]. Varol et al. [69] suggested that polydopamine facilitates the control of ion transport by regulating the pH-dependent accessibility of nanopores. The molecular origins of surface chemical and electronic structural changes induced by DA-treatment in 1T-TiS_2 are explored through Ti2p XPS data (Fig. S10, Supporting Information). The Ti2p XPS data revealed major features at 456.3 and 458.8 eV, corresponding to TiS_2 and TiO_2 in 1T-TiS_2 film [70,71]. In DA-TiS_2, an abundance of TiO_2 surface domains indicates a transformation of TiS_2 to TiO_2. Molecular-level changes upon DA treatment is explained by auto-oxidation and polymerization of DA. H_2O_2 generation during the DA auto-redox reaction is crucial for structural alterations, converting TiS_2 to TiO_2[68]. The thin TiO_2 overlayer passivated the surface, improving structural stability without affecting electrochemical functionality. In addition, the lack of XRD signals of thick and ordered titania domains for DA-TiS_2 in Fig. 1g served as evidence that the thin TiO_2 overlayer is exceptionally thin [72]. S2p XPS data (Fig. S11, Supporting Information) revealed three S2p states in surfaces of 1T-TiS_2 and DA-TiS_2 films, showing an increase in sulfur species with higher oxidation states after DA treatment, correlating with the expected oxidizing action of in-situ generated H_2O_2 [70,73]. O1s XPS data (Fig. S12, Supporting Information) indicated an intensified high binding energy shoulder at 532.5 eV after DA treatment, consistent with increased O1s states from oxygen atoms in DA and the formation of a TiO_2 overlayer on TiS_2. The ATR-IR spectra of 1T-TiS_2 and DA-TiS_2 films (Figs. S13(a–b), Supporting Information) revealed weak but detectable signals, indicating the presence of small amounts of DA and its derivatives on the TiS_2 surface. The incomplete polymerization of DA and the observed hydrophobicity of the TiO_2 surface contributed to the enhanced stability of the DA-TiS_2 under electrochemical conditions. A detailed explanation of these findings is shared in Supporting Information. In short, it is argued that DA treatment forms a disordered thin TiO_2 overlayer due to auto redox reaction caused by H_2O_2. This thin TiO_2 overlayer suppressed the degradation of the 1T-TiS_2 structure in an aqueous environment, which is practically observed in Fig. 1f and evaluated in detail through electrochemical characterizations.

The electrochemical behavior of 2D 1T-TiS_2 electrodes is assessed by drop-casting 300 μg of a TiS_2 suspension onto indium tin oxide (ITO) thin film (sheet resistance of 10 Ω sq^{-1}) coated glass substrates (electrodes). Cyclic voltammetry measurements in three-electrode configuration are conducted with different electrolytes to determine the best one with highest compatibility. 1 M concentrations of sulfuric acid (H_2SO_4), potassium hydroxide (KOH), lithium sulfate (Li_2SO_4), sodium sulfate (Na_2SO_4), and sodium chloride (NaCl) electrolytes are used for this purpose. The resulting cyclic voltammograms are provided in Fig. 2a. 2D 1T-TiS_2 was not stable in the acidic environment of H_2SO_4, while similar results are obtained for both basic and neutral electrolytes (KOH, Li_2SO_4, Na_2SO_4), and NaCl. Best performing electrolytes are assessed as NaCl and Li_2SO_4. It is known that electrolytes consisting of chloride ions could cause pitting on the surface of the stainless-steel current collectors, affecting the devices' long-term stability. Therefore, 1M Li_2SO_4 is chosen as the electrolyte [74]. At a scan rate of 200 mV s^{-1}, through the use of 1M Li_2SO_4 electrolyte within a potential window of −0.8 to −0.2 V, a specific capacitance of 80 F g^{-1} is obtained (Fig. 2a). In the rest of the study Li_2SO_4 is used as the main electrolyte, and further optimization is done based on this selection.

Symmetric supercapacitor devices are fabricated with the chosen 1 M Li_2SO_4. Detailed analysis of the behavior and stability of the devices are provided in Figs. S14–S16, Supporting Information. An activation step is performed over 400 CV cycles, and the resulting voltammogram is given in Fig. S14, Supporting Information. Upon activation, capacitance is enhanced. This was due to the reaction couple which appeared during the activation. The appearance of the reaction couple is correlated with the interlayer expansion of TiS_2 due to Li^+ insertion and the partial oxidation of TiS_2 layers. The effect of the reaction couple was also visible in the charge-discharge curves of galvanostatic charge-discharge (GCD) measurements (Fig. S15, Supporting Information). Cycling of the symmetric cells after the activation step is done to observe the cells' stability. Without the DA functionalization and electrolyte optimization, symmetric 1T-TiS_2 cell could not retain its initial capacitance (Fig. S16, Supporting Information). Detailed information on activation and stability is given in Supporting Information.

These results indicated the need for stability improvement. As mentioned before, TiS_2 had low oxidation resistance in the presence of water and oxygen. Ursi et al. [75] reported that introducing amine groups could enhance the oxidation stability of TiS_2 through substituting the amine groups with sulfur (S) vacancies. TiS_2 with enhanced stability is then used as an n-type thermoelectric material. Moreover, Ko et al. [64] demonstrated surface functionalization with ligands to improve the

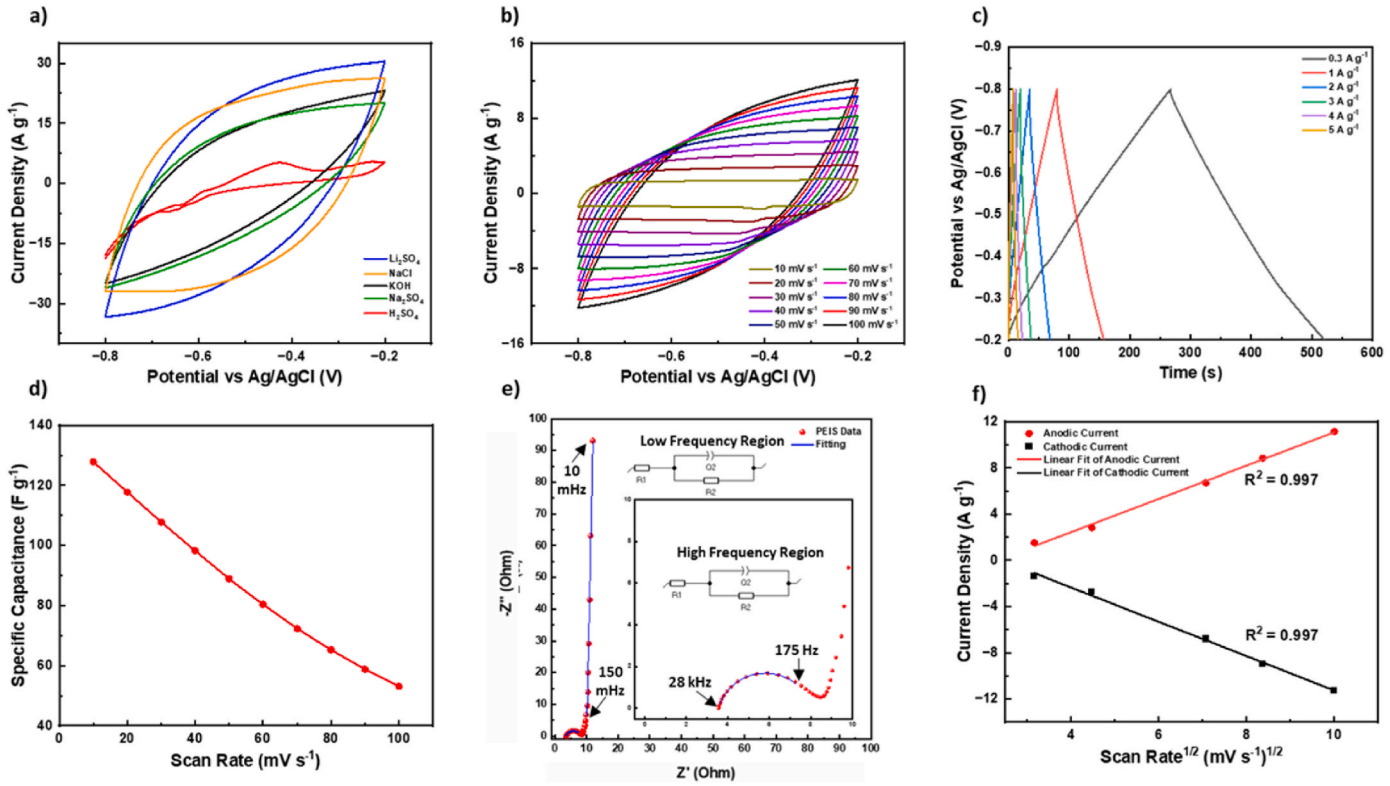

Fig. 2. Three-electrode measurements of 1T-TiS_2 electrodes. a) CV measurements of 1T-TiS_2 in different electrolytes. b) CV plot of DA-treated 1T-TiS_2 in three-electrode configuration at various scan rates. c) GCD profile of the electrode. d) Specific capacitances of the electrode at various scan rates. e) EIS results of the electrode. f) Coefficient of determination (R^2) values for anodic and cathodic current.

oxidation stability of titanium carbide (Ti_3C_2 -MXene), another 2D and layered material. In addition, Ko et al. suggested that adsorbed functional groups could act to passivate the surface, preventing water molecules from reaching it and thereby enhancing the capacitive efficiency of MXene. Inspired by these studies, we have treated 2D 1T-TiS_2 electrodes with DA (DA-treated 1T-TiS_2 electrodes: DA-TiS_2). For this purpose, the amount of 1T-TiS_2 is kept constant (40 mg) in Tris-HCl solution, where different amounts of DA hydrochloride are added to these suspensions. Detailed instructions and electrode optimization processes are provided in the **Experimental Section** and Supporting Information. It is observed that the introduction of DA inhibited the detrimental interaction between TiS_2 and water, leading to a notable enhancement in electrochemical cyclic stability of the currently prepared devices (Figs. S17(a–c), Supporting Information). Moreover, no significant changes in Nyquist plots are observed (Fig. S18(a-c), Supporting Information), indicating the enhanced stability of TiS_2 electrodes. These results readily align with the XPS results and the earlier explanation of TiS_2 passivation through thin TiO_2 coverage with the DA functionalization. Excess DA introduction seemed to further decrease the specific capacitance of the supercapacitor devices. Thanks to its outstanding initial performance, electrodes fabricated using 8 mg of DA hydrochloride are used for the subsequent device optimization efforts.

The electrolyte of the supercapacitors, fabricated with DA-TiS_2 electrodes, is also modified to further enhance the cyclic stability of the supercapacitors. Thiourea is chosen as an additive due to its amine group, which, as previously mentioned, contributes to the stabilizing effect of the materials with the amine group [75]. 2 M Li_2SO_4 electrolyte was modified through the addition of 0.1 M thiourea to improve the cyclic stability of the devices. Cyclic voltammetry measurements of DA-TiS_2 using a modified electrolyte were conducted at a scan rate of 100 mV s^{-1}. It was apparent that adding thiourea to the electrolyte further increased the stability of 1T-TiS_2 electrodes. A superior cyclic stability of 93.3 % was obtained for DA-TiS_2. Therefore, 1T-TiS_2 electrodes treated with 8 mg DA (DA-TiS_2) in combination with 2 M Li_2SO_4 electrolyte with 0.1 M thiourea are used in subsequent studies, including three-electrode and symmetric device measurements.

Following the optimization of the electrodes and the electrolyte, electrochemical storage characteristics of the treated electrodes are investigated in the three-electrode system using 2 M of aqueous Li_2SO_4 electrolyte with a thiourea additive of 0.1 M (Fig. 2b–f). The rectangular CV shape of the electrode within a potential range of −0.2 to −0.8 V (vs. Ag/AgCl) at various scan rates (Fig. 2b) indicated the capacitive behavior of the electrode [76]. Specific capacitance and Coulombic efficiency (CE) calculations are made using Equation (1) and 2, respectively [77].

$$C_{sp} = \frac{\int I.dV}{2\nu mV} \tag{1}$$

$$CE = \frac{t_d}{t_c} \tag{2}$$

For Equation (1), C_{sp} corresponds to specific capacitance (F g^{-1}), while I and V represent instantaneous current (mA) and potential range (V), respectively. ν is the scan rate (mV s^{-1}), and m is the mass of active material. For Equation (2), t_d and t_c correspond to discharging and charging time (sec), respectively. A maximum specific capacitance of 128 F g^{-1} is obtained at a scan rate of 10 mV s^{-1}. Moreover, a maximum volumetric capacitance of 122 F cm^{-3}, and an areal specific capacitance of 244 mF cm^{-2} are obtained. GCD measurements are conducted at different current densities to figure out the charge storage performance of DA-TiS_2 electrodes. GCD measurements resulted in triangular-shaped profiles at all current densities, proving high Coulombic efficiency. Maximum Coulombic efficiency of (CE) 96 % is obtained at a current density of 2 A g^{-1} (Fig. 2c) [78]. Additionally, a specific capacitance of 133.6 F g^{-1} is achieved at a current density of 0.3 A g^{-1}.

The high reversibility of the fabricated supercapacitors is demon-

strated through their remarkable Coulombic efficiency. The rate capability of the electrode is shown in Fig. 2d. The consistent inverse correlation between scan rate and specific capacitance aligned with the underlying charge storage mechanism of supercapacitors, which enabled better ion adsorption and higher specific capacitance at slower scan rates, which can be correlated with the pseudocapacitive behavior. An almost linear relation between the scan rate and specific capacitance further complements its ideal pseudocapacitive behavior. Potentiostatic electrochemical impedance spectroscopy (PEIS) analysis is conducted to further understand the working mechanism of the supercapacitors utilizing DA-TiS_2. The resulting Nyquist plot is given in Fig. 2e, and relevant fitting is made using the EC-Lab software. The inset shows two different fittings of constant phase element (CPE – Q_2) with parallel resistances. Detailed results of the fittings are provided in Supporting Information, in Table S1. The rationale behind the two separate fittings lies in the association of the complex region between 175 Hz–150 mHz frequencies with the porous structure of the vacuum-filtered 1T-TiS_2 film. Vacuum filtration resulted in a packed layered structure (see Fig. 1a–b), effectively limiting ionic migration. The high-frequency region is attributed to the electrode/electrolyte interface [79]. The low value of R_1, $\approx 3.5\,\Omega$ was the indication of the high electrical conductivity of self-standing and binder-free 1T-TiS_2 electrodes, supportive of 4-probe measurement results. The small semicircle with the repressed shape was the indication of a CPE element Q_2, with a minimal capacitive contribution. For the low-frequency region, the same CPE model is used. A high α constant value of 0.986 indicated a near-ideal capacitive behavior of the 1T-TiS_2 electrodes. The capacitive contribution, measuring 280 mF, corresponded to a capacitance value of 180 F g^{-1}, closely approximating the value obtained through CV (Fig. 2b). Very high resistance in the range of $10^{15}\,\Omega$ is obtained from the CPE model in the low-frequency region, possibly indicating exceptional leakage resistance. Current density vs square root of scan rate plots is fitted for

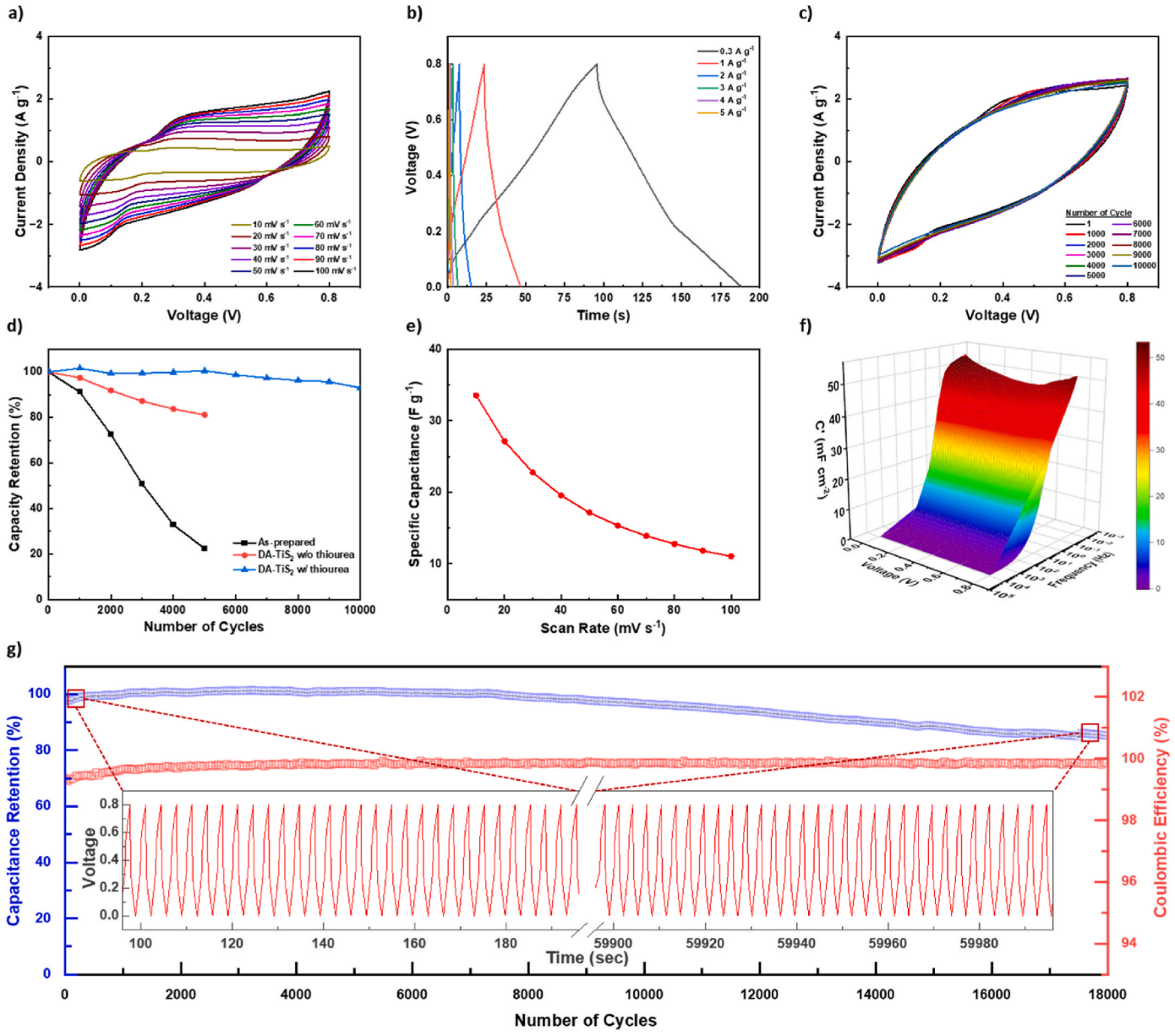

Fig. 3. Electrochemical characterization of symmetric supercapacitor devices. a) CV plot for DA-TiS_2 at various scan rates. b) GCD profile for DA-TiS_2 at various current densities. c) CV plots for 10000 cycles showing the stability. d) Capacity retentions of devices using as-prepared and DA-TiS_2 electrodes with and without thiourea. e) Specific capacitance of the device at various scan rates. f) 3D Bode plot map. g) Capacitance retention and Coulombic efficiency graph with a current density of 2 A g^{-1} for 18000 cycles. The inset graph shows the charge-discharge curves from the initial and final parts of the GCD measurement.

anodic and cathodic currents (Fig. 2f). From the Randles-Sevcik plot, an R2 value of 0.997 is obtained from linear fitting for both anodic and cathodic current up to 100 mV s^{-1}, demonstrating high reversibility of the electrodes [80].

Following the electrochemical characterization of DA-TiS_2 in three-electrode configuration, symmetric cells are assembled. Cyclic voltammetry (CV) measurements are conducted at various scan rates within a potential window of 0–0.8 V for symmetric cells, the results of which are provided in Fig. 3a. The rectangular-like shape of the CV curve indicated ideal pseudocapacitive behavior [81]. The shape of the CV curve is distorted with an increased scan rate due to diffusion limitations [82]. Nevertheless, assembled symmetric supercapacitors could work up to a scan rate of 500 mV s^{-1} without suffering much from internal resistance (IR) (Fig. S19, Supporting Information). Galvanostatic charge-discharge (GCD) analysis is conducted using current densities ranging from 0.3 to 5 A g^{-1} to investigate the charge-discharge mechanism of the symmetric cells (Fig. 3b). A Coulombic efficiency of 99.7 % is obtained at a current density of 3 A g^{-1}. GCD profiles with triangular shapes indicated significant capacitive contribution with outstanding reversibility during charge and discharge [83,84]. A specific capacitance of 35.2 F g^{-1} is calculated from the GCD profile at a current density of 0.3 A g^{-1}.

High-capacity retention is paramount for the reliability and sustainability of a supercapacitor device. 10000 cycles of cyclic stability test are performed through CV measurements at a scan rate of 100 mV s^{-1} (Fig. 3c). A capacitance retention of 93.3 % was obtained after 10000 cycles. Following 10000 cycles of cyclic stability test, a Coulombic efficiency of 97.6 % is maintained at a current density of 0.3 A g^{-1} (Fig. S20, Supporting Information). Demonstration of the improved capacity retention with the applied modifications is shown through the CV plot provided in Fig. 3c. Initially, we achieved a remarkable improvement in capacity retention through the DA treatment. Retention is increased from 22.4 % (as-prepared) to 81.1 % (without thiourea) following 5000 charge/discharge cycles as a consequence of the DA modification. Subsequently, with the addition of thiourea to the electrolyte, capacity retention is further improved to 93.3 %. The resulting capacitance retention graphs are given in Fig. 3d, showcasing the improved retention upon thiourea optimization. The initial specific capacitance of 1T-TiS_2 was 31.9 F g^{-1}, decreasing to 7.15 F g^{-1} after 5000 cycles, while DA-TiS_2 started at 12.6 F g^{-1} and retained 11.76 F g^{-1} after 10000 cycles. PEIS analysis of DA-TiS_2 symmetric supercapacitor with thiourea addition is also conducted both before and after 10000 cyclic voltammetry cycles (Fig. S21, Supporting Information). Electrode resistance is measured as 3.1 Ω prior to cycling, which is found to increase to 3.9 Ω after cycling. This increase was almost negligible for 10000 continuous cycles. Specific capacitance values of these cells are plotted with respect to the scan rate and provided in Fig. 3e. A maximum specific capacitance of 33.5 F g^{-1} at a scan rate of 10 mV s^{-1} is obtained.

To further explore the behavior of DA-treated 1T-TiS_2 electrodes, a 3D Bode plot is constructed through PEIS measurements at small applied potential intervals of 20 mV, up to 0.8 V. Real capacitance (C') with respect to applied voltage and frequency is plotted for the 3D Bode plot (Fig. 3f). In a comprehensive analysis conducted by Ko et al. [85], storage mechanisms for different materials were elaborated using 3D Bode analysis. Based on the work by Ko et al. [85], and considering the 3D Bode plot, 1T-TiS_2 is found to behave as a pseudocapacitive material. This further supported the findings from the Nyquist plot (Fig. 2e) as well as the shapes of CV (Fig. 3a) plots and GCD (Fig. 3b) profiles. Furthermore, Fleischmann et al. [86] have demonstrated the existence of non-diffusion limited lithiation due to expanded TiS_2 interlayer spacings, which is in good agreement with the observed mechanism in this work. Hence, it became evident that with appropriate fabrication and modifications, 2D structures of 1T-TiS_2 hold substantial promise for supercapacitor applications and energy storage. A Ragone plot is also constructed and provided in Fig. S22, Supporting Information. Specific energy density (E) and specific power density (P) are calculated according to the GCD curves in Fig. 3b using Equations (4) and (5) given below;

$$E = \frac{1}{2} C_{sp} V^2 \quad \left(\text{Wh kg}^{-1}\right) \tag{4}$$

$$P = \frac{E}{\Delta t} \left(\text{W kg}^{-1}\right) \tag{5}$$

where C_{sp} was calculated from Equation (6);

$$C_{sp} = \frac{i \Delta t}{V} \tag{6}$$

where i is the current density (A g^{-1}) and Δt is the discharge time. From here, maximum P and E values are calculated as 2000 W kg^{-1} and 3.1 Wh kg^{-1}, respectively. Within the Ragone plot, it's evident that optimized 1T-TiS_2 symmetric supercapacitors reside at the high end of the electrochemical supercapacitor spectrum [87]. This further proved that 1T-TiS_2 electrodes, when carefully engineered for stability, are capable of delivering high performance, holding promise for future energy storage applications.

Stability tests of devices fabricated with DA-treated 1T-TiS_2 are conducted using GCD measurements to demonstrate their potential for real-world applications. Relevant graph, including capacitance retention and Coulombic efficiency, is provided in Fig. 3g. At the current density of 2 A g^{-1}, a capacitance retention of 96.1 % is achieved after 10000 charge-discharge cycles, which is extended to a retention of 85.5 % after 18000 cycles. The Coulombic efficiency during the measurement is almost 100 %, signifying good supercapacitive behavior. After 18000 cycles at 2 A g^{-1}, further GCD measurements ranging from 2 A g^{-1} to 0.1 A g^{-1} are conducted per each 50 cycles. Respective graph is given in Fig. S23, Supporting Information. A specific capacitance of 31.2 F g^{-1} is achieved at a current density of 0.1 A g^{-1}, showing that the supercapacitor devices with DA-treated 1T-TiS_2 still retain their capacity after long-term usage. The results were in good agreement with the stability measurements conducted with CV and prove that the DA-treated 1T-TiS_2 electrodes can be utilized in real-case scenarios.

Self-discharge is one of the most important occurrences that might significantly reduce the device performance due to a potential decrease [88]. Self-discharge behavior of the fabricated supercapacitors is monitored, the result of which is provided in Fig. S24, Supporting Information. A constant potential of 0.8 V is applied for 1 min to ensure the supercapacitor device is fully charged. Then, the open-circuit voltage (OCV) of the device is monitored for 1 h. It took 10 min for the supercapacitor to drop from 0.8 V to ~ 0.6 V. Later, it took 50 min for the 1T-TiS_2 supercapacitor to drop from 0.6 V to ~ 0.4 V, showing excellent leakage resistance. This leakage resistance can be correlated with the high leakage resistance R_4 from the fitting provided in Fig. 2d. In the pseudocapacitive charge storage mechanism, some ions in the electrolyte undergo a faradaic reaction, and ions are tightly adsorbed on the surface of the electrode [89]. Desorption of ions is more difficult for those tightly adsorbed ions, and such high leakage resistance is related to the pseudocapacitive behavior of 1T-TiS_2.

To understand the structural changes in 1T-TiS_2 and DA-TiS_2 electrodes, SEM, XRD and XPS analyses are conducted after 10000 cycles of cyclic voltammetry. SEM images of the positive and negative electrodes of 1T-TiS_2 and DA-TiS_2 in symmetric devices are analyzed, before and after cycling. It is observed that the sheet-like structures in the 1T-TiS_2 electrodes are completely degraded, while they remained intact in the DA-TiS_2 electrodes (Fig. S25, Supporting Information). As shown in Fig. S26, Supporting Information, additional XRD peaks corresponding to the (004) plane of anatase phase of hydrated TiO_2 are observed in 1T-TiS_2 positive electrode (1T-Positive) [90]. New peaks in the XRD patterns were associated with $Ti(OH)_4/TiO_2$, rather than a pure crystalline TiO_2 [91]. XPS results revealed the highest intensity increase in the O 1s signal for the 1T-Positive electrode, followed by the 1T-Negative electrode (Fig. S27, Supporting Information). Compared to the DA-TiS_2

electrodes, this increased oxygen species suggested that the stability issues observed in the 1T-TiS_2 electrodes may be attributed to this hydrated form. Surface atomic concentrations of 1T-TiS_2, DA-TiS_2, 1T-Positive, 1T-Negative, DA-Positive and DA-Negative are given in Fig. S28, Supporting Information. The surface atomic concentration of oxygen in the as-prepared 1T-TiS_2 electrode is measured as 15.2 %, whereas in the 1T-Positive electrode, it increased up to 40.3 %. In the case of DA-treated electrodes, the controlled oxidation on the surface of as-prepared DA-TiS_2 is 28.7 %, which increased to 41.6 %. Much lower increase in the oxygen concentration of DA-Positive electrodes compared to 1T-Positive electrodes with respect to their initial states proved the successful passivation of the TiS_2 structures. These findings are consistent with the results from SEM and XRD analyses, further indicating that the 1T-Positive electrode served as the limiting electrode in terms of stability. Furthermore, a substantial reduction in the surface atomic concentration of sulfur has been observed. The absence of lithium in the as-prepared electrodes suggests that no lithiation occurred during the exfoliation process, and no residual lithium remained. However, XPS analysis also revealed a small degree of lithium intercalation in the DA-Negative electrode. A detailed summary of surface atomic concentration percentages is provided in Table S2, Supporting Information. Moreover, the relatively lower oxygen intensity in the DA-TiS_2 electrodes indicates that dopamine treatment provides protection against this aforementioned formation of hydrated $Ti(OH)_4/TiO_2$. In the S2p region of XPS spectra (Fig. S29, Supporting Information), S^{2-} states attributed to TiS_2, polysulfide (S_x^{2-}) ions, and oxidized SO_x species (predominantly S^{6+} states from SO_4^{2-}, with a smaller contribution from S^{4+} states due to SO_3^{2-}) are located at approximately 161.0 eV, 163.0 eV, and 169.0 eV, respectively [73,92]. The increased signals of polysulfide and oxidized SO_x species in the 1T-Positive electrode highlight the stability issue of the 1T-Positive electrode, as these species are the primary contributors to electrode degradation. All in all, dopamine functionalization of the 1T-TiS_2 proved to be an efficient way to prevent degradation of TiS_2, allowing aqueous symmetric supercapacitor devices to be stable over extended cycling periods.

Coin cells are prepared for use in series, parallel, and both series and

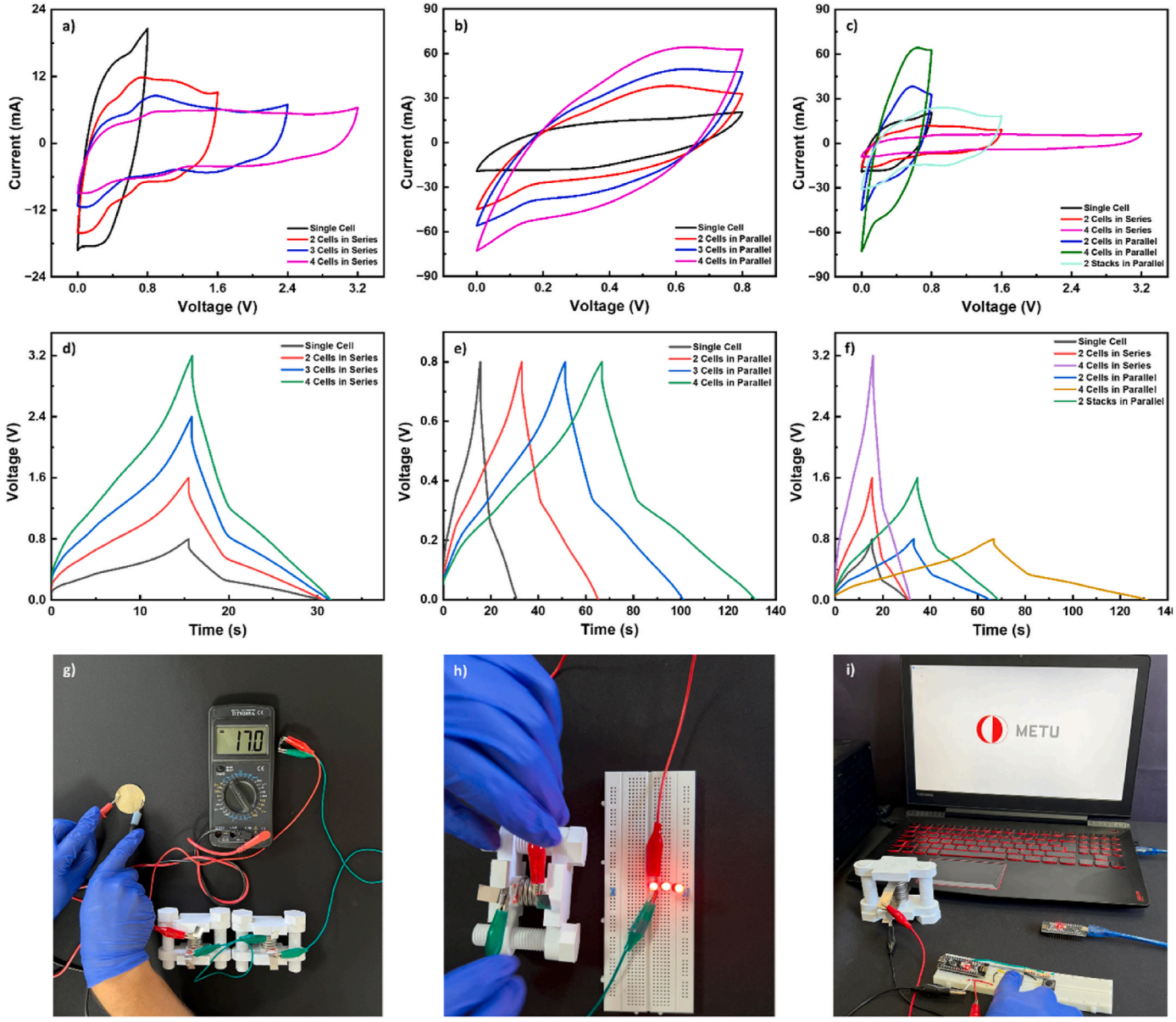

Fig. 4. CV measurement results of a) series and b) parallel-connected coin cells. c) CV comparisons of series, parallel, and both series and parallel-connected coin cells. GCD profiles of d) series and e) parallel-connected coin cells. f) GCD comparisons of series, parallel, and both series and parallel-connected coin cells. 1T-TiS_2 supercapacitor powered g) multimeter, h) LED bulbs and i) RFID.

parallel connections. 2032 cells are used for this purpose. DA-treated 1T-TiS_2 electrodes are punched in 10 mm diameter, and 0.1 M thiourea containing 2 M $LiSO_4$ is used as the electrolyte. CV plots and GCD profiles of series and parallel-connected coin cells are provided in Fig. 4a–f. Two stacks, each made up of two series-connected cells, are also connected in parallel and named as "2 Stacks in Parallel". The voltage of the assembly is proportionally increased through serially connected cells while it is kept constant at 0.8 V for parallel connections. (Fig. 4a–b). In series-connected cells, energy density remained the same regardless of the number of connected cells. Conversely, increasing the number of parallel-connected cells resulted in a proportional rise in energy density, aligning with expectations. The consistent outcomes observed in both series and parallel connection variations highlight the repeatability of device fabrication and indicate negligible losses during the connections of coin cells (Fig. 4c). As expected, charge and discharge times remained the same regardless of the number of series-connected cells (Fig. 4d). In turn, charge and discharge times increased proportionally for parallel-connected cells (Fig. 4e). After these measurements, coin cells are connected in series, and a supercapacitor stack is obtained. A supercapacitor stack formed with 10 symmetric cells is charged with a power supply and then used to power up a multimeter that generally works with a 9-V battery. The multimeter is turned on, its internal resistance is measured, and then it is used to measure the resistance of a self-standing 1T-TiS_2 film (Fig. 4g–Supplementary Video 1). Similarly, 3 LEDs are lit thanks to a directly connected stack of 5 serially connected cells (Fig. 4h–Supplementary Video 2). Finally, 1T-TiS_2-powered RFID (Radio Frequency Identification) is turned on, which allowed sending signals to the computer to change the marks on the screen. (Fig. 4i–Supplementary Video 3). The impressive capabilities of 1T-TiS_2-based symmetric supercapacitors, as demonstrated in their ability to power everyday devices and enable RFID technology, highlight their significant promise for practical applications.

There are only limited number of studies on the use of TiS_2 nanosheets in supercapacitor applications in the literature. The scarcity of existing research underscores the importance of conducting thorough investigations to unveil the full capabilities of TiS_2 nanosheets as supercapacitor electrodes. Zang et al. [93] fabricated symmetric supercapacitor devices using nanocomposites of vertically aligned carbon nanotubes (VACNTs) coated with pseudocapacitive TiS_2. The atomic layer deposition (ALD) method was used for the deposition of titanium onto VACNTs, followed by sulfurization. A power density of 1250 W kg^{-1} was reported using aqueous 21 M lithium trifluoromethanesulfonate (LiTFSI) electrolyte. Tang et al. [94] utilized MXene-derived TiS_2 nanosheets with the assistance of hydrogen sulfide (H_2S) gas. Fabricated non-aqueous sodium-ion capacitors achieved a power density of 200 W kg^{-1} and a capacity retention of 92.5 % after 5000 cycles. Chaturverdi et al. [95,96] proposed TiS_2 as an insertion host material for non-aqueous lithium-ion and sodium-ion capacitors. The aforementioned studies relied on bulk TiS_2 for the fabrication of electrodes, making use of conductive additives and binders to facilitate energy storage. None of them utilized semimetallic and self-standing 1T-TiS_2 nanosheets. In a recent study, aqueous 2 M LiTFSI electrolyte was employed for TiS_2/Lithium iron phosphate ($LiFePO_4$) based Li-ion battery. Yet, after 500 cycles, only 62 % of the discharge capacity could be retained, once again highlighting the degradation [97]. Our study not only shows the promise in 2D 1T-TiS_2 obtained through organolithium exfoliation for energy storage devices but also puts forth a feasible way for stabilizing them in aqueous environments. It is crucial to utilize and unlock the great potential of 1T-TiS_2 in energy storage devices, as this work has highlighted through achieving a power density of 2000 W kg^{-1} and a capacity retention of 93.3 % after 10000 cycles.

3. Conclusions

In conclusion, bulk TiS_2 powders produced by annealing titanium and sulfur powders were exfoliated using n-butyllithium. Characterizations confirmed the successful production of 2D 1T-TiS_2 nanosheets. The proposed stable pathway for 2D TiS_2 holds promise for future commercialization. However, scalability remains a challenge, with the exfoliation process—rather than the dopamine treatment—being the primary limiting factor. Though improvements are required, they are within reach. Oxidation-resistant, binder-free, self-standing 1T-TiS_2 electrodes with high electrical conductivity were fabricated and used in symmetric supercapacitor devices. The aqueous stability of 2D 1T-TiS_2 electrodes was significantly improved via DA treatment through the formation of a thin TiO_2 overlayer functionalized by DA. The resulting DA-TiS_2 electrodes were utilized in symmetric supercapacitor devices with aqueous electrolytes. A maximum Coulombic efficiency of 99 % from fabricated devices and a capacity retention of 96.1 % were obtained after 10000 cycles. Furthermore, coin cells were assembled to power a multimeter, LEDs, and RFID, showcasing the potential of TiS_2 supercapacitors for real-world applications. The successful development of durable and high-performance 1T-TiS_2 electrodes, with their outstanding capacity retention and electrochemical versatility, opens up promising opportunities for advanced energy storage applications. 2D 1T-TiS_2 is expected to play a significant role in cutting-edge energy applications, including electronics, batteries, and supercapacitors, providing a sustainable alternative for the ever-evolving energy needs.

4. Experimental section

Fabrication of 2D TiS_2 Flakes: Titanium (99.9 %, Nanografi Co. Inc) and sulfur (99.98 %, Sigma Aldrich) powders were mixed and annealed at 650 °C for 18 h in a vacuumed quartz tube. Then, 0.5 g of TiS_2 powder and 10 ml n-butyllithium (1.6 M in hexane, Sigma Aldrich) were stirred in a sealed autoclave at 80 °C for 48 h. Lithium-intercalated TiS_2 powders were washed through centrifuging three times each with hexane, ethanol, and deionized water at 11000 rpm for 30 min. Lithium-intercalated TiS_2 powders were added to 300 ml of deionized water and ultrasonicated in an ice bath for 4 h. After washing twice with water, the concentrated product (1 mg/ml) was stored in ethanol for further use.

Fabrication of Self-standing SWCNT//TiS_2 Films: First, 0.25 g of sodium dodecyl sulfate (SDS, 99.0 %, Sigma-Aldrich) was added to 100 ml of deionized water and sonicated using a tip-sonicator for 5 min to dissolve SDS. Then, 10 mg of SWCNTs (P3-SWNT, Carbon Solutions Inc.) was added to the SDS solution and sonicated for 5 min to ensure proper dispersion. 20 ml of SWCNT solution was added dropwise to 40 ml of 1 mg/ml concentrated TiS_2 solution and stirred vigorously at room temperature for 1 h. Self-standing and flexible TiS_2 films were obtained through vacuum filtration. Hydrophobic PTFE membrane filters (0.45 μm, ISOLAB) were used for filtration. Self-standing films were punched to obtain 1 cm diameter electrodes for supercapacitors.

Fabrication of DA-treated Self-standing SWCNT//TiS_2 Films: 40 mg of TiS_2 was dispersed in 10 ml of 8.5 pH and 0.1 M Tris (Tris(hydroxymethyl)aminomethane)-HCl (Extrapure AR) buffer solution. Dopamine hydrochloride was added to the solution and stirred for 1 h. The product was washed by centrifuging two times with deionized water. Finally, the product was dispersed in ethanol. The steps of SWCNT addition, vacuum filtration, and punching were the same for DA-treated films as above.

Characterizations and Measurements: Conductivity measurements were conducted using a Signatone Pro4 4-point probe testing station with a Keithley 24000 sourcemeter. Absorbance analysis was performed using Shimadzu UV-3600 UV–VIS–NIR Spectrophotometer. SEM analysis was carried out using FEI Nova Nano FEG-SEM. XRD analysis was performed using a Rigaku D/Max-2000 diffractometer employing Cu Kα radiation at an operating voltage of 40 kV, within the range of 10–90°, and a scanning rate of 2°/min. High-resolution (HR-TEM JEOL JEM-2100F) and high-contrast (HC-TEM FEI Tecnai G^2 Spirit BioTwin) TEM analyses were performed with 200 and 120 kV operating voltages, respectively. TEM samples were prepared simply by drop-casting the samples onto holey carbon-coated 400 mesh copper grids. XPS

experiments were conducted with a SPECS HSA3500 hemispherical energy analyzer and a PHOIBOS 100 detector with an MCD-5. During the XPS data acquisition, a monochromatic Al-Kα X-ray excitation source (14 kV, 350 W, 1486.6 eV, Ag $3d_{5/2}$ full width at half-maximum (FWHM) = 0.90 eV, pass energy 20 eV) was employed along with an electron flood gun for charge compensation. Short acquisition time (control) spectra were recorded at the beginning and end of each experiment to ensure that the samples did not suffer from degradation during the measurements. Binding energy (B.E.) values of the XP spectra were shifted to the C1s line of the adventitious carbon at 284.5 eV. XPS data analysis was conducted via the CasaXPS software, and background subtraction was performed using a Shirley background. XPS peak deconvolution was performed via a weighted least-squares fitting method using 70 % Gaussian and 30 % Lorentzian line shapes. The surface atom % values were quantified using Scofield's relative sensitivity factors. Raman spectroscopic measurements were performed using Witec UHTS 600 Via Raman Spectrometer with a 532 nm laser and 4 cm^{-1} resolution. ATR-IR spectra were acquired via a Bruker Alpha spectrometer using 256 scans and 4 cm^{-1} resolution. Electrochemical measurements were conducted using a VMP-3 Biologic potentiostat/galvanostat system. In a three-electrode configuration, Ag/AgCl and platinum electrodes were used as reference and counter electrodes, respectively. Symmetric supercapacitor devices were fabricated using Swagelok cells with a Whatman cellulose-based filter paper separator. 2032 coin cells were assembled for device integrations.

CRediT authorship contribution statement

Ali Deniz Ucar: Writing – review & editing, Writing – original draft, Methodology, Investigation, Formal analysis, Data curation. **Sumeyye Kandur Baglicakoglu:** Writing – review & editing, Writing – original draft, Investigation, Data curation. **Mete Batuhan Durukan:** Writing – review & editing, Writing – original draft, Visualization, Methodology, Investigation, Formal analysis, Data curation, Conceptualization. **Murathan Cugunlular:** Writing – review & editing, Writing – original draft, Formal analysis, Data curation, Conceptualization. **Sena Oz:** Writing – review & editing, Writing – original draft, Data curation, Conceptualization. **Yusuf Kocak:** Writing – review & editing, Writing – original draft, Visualization, Software, Methodology, Investigation, Formal analysis, Data curation, Conceptualization. **Burak Ülgüt:** Writing – review & editing, Writing – original draft, Software, Investigation. **Emrah Ozensoy:** Writing – review & editing, Writing – original draft, Software, Resources, Methodology, Investigation, Data curation, Conceptualization. **Husnu Emrah Unalan:** Writing – review & editing, Writing – original draft, Supervision, Resources, Conceptualization.

Declaration of competing interest

The authors declare that they have no known competing financial interests or personal relationships that could have appeared to influence the work reported in this paper.

Acknowledgments

Melis Ercan is acknowledged for her valuable support in graphical design throughout this work. Onur Demircioğlu is acknowledged for his support in the bending measurements.

Appendix A. Supplementary data

Supplementary data to this article can be found online at https://doi.org/10.1016/j.mtener.2025.101810.

Data availability

Data will be made available on request.

References

[1] M.D. Stoller, S. Park, Y. Zhu, J. An, R.S. Ruoff, Graphene-Based Ultracapacitors, 2008, pp. 6–10.
[2] H.P. Wu, D.W. He, Y.S. Wang, M. Fu, Z.L. Liu, J.G. Wang, H.T. Wang, Graphene as the electrode material in supercapacitors. Proceedings - 2010 8th International Vacuum Electron Sources Conference and Nanocarbon, IVESC 2010 and NANOcarbon, 2010, pp. 465–466, https://doi.org/10.1109/IVESC.2010.5644267, 2010.
[3] Y. Wang, Z. Shi, Y. Huang, Y. Ma, C. Wang, M. Chen, Y. Chen, Supercapacitor devices based on graphene materials, J. Phys. Chem. C 113 (30) (2009) 13103–13107, https://doi.org/10.1021/jp902214f.
[4] Q. Zhu, D. Zhao, M. Cheng, J. Zhou, K.A. Owusu, L. Mai, Y. Yu, A new view of supercapacitors: integrated supercapacitors, Adv. Energy Mater. 9 (36) (2019) 1–11, https://doi.org/10.1002/aenm.201901081.
[5] S. Ghosh, S. Barg, S.M. Jeong, K. Ostrikov, Heteroatom-doped and oxygen-functionalized nanocarbons for high-performance supercapacitors, Adv. Energy Mater. 10 (32) (2020), https://doi.org/10.1002/aenm.202001239.
[6] Patrice Simon, Gogotsi Yuri, Bruce Dunn, Where do batteries end and supercapacitors begin? Science 343 (6176) (2014) 1208–1210, 1979.
[7] K. Jost, D.P. Durkin, L.M. Haverhals, E.K. Brown, M. Langenstein, H.C. De Long, P. C. Trulove, Y. Gogotsi, G. Dion, Natural fiber welded electrode yarns for knittable textile supercapacitors, Adv. Energy Mater. 5 (4) (2015) 1–8, https://doi.org/10.1002/aenm.201401286.
[8] K. Jost, G. Dion, Y. Gogotsi, Textile energy storage in perspective, J Mater Chem A Mater 2 (28) (2014) 10776–10787, https://doi.org/10.1039/c4ta00203b.
[9] L. Liu, Z. Shen, M. Yi, X. Zhang, S. Ma, A green, rapid and size-controlled production of high-quality graphene sheets by hydrodynamic forces, RSC Adv. 4 (69) (2014) 36464–36470, https://doi.org/10.1039/C4RA05635C.
[10] S. Liu, K.S. Hui, K.N. Hui, Flower-like copper cobaltite nanosheets on graphite paper as high-performance supercapacitor electrodes and enzymeless glucose sensors, ACS Appl. Mater. Interfaces 8 (5) (2016) 3258–3267, https://doi.org/10.1021/acsami.5b11001.
[11] E. Dhandapani, S. Thangarasu, S. Ramesh, K. Ramesh, R. Vasudevan, N. Duraisamy, Recent development and prospective of carbonaceous material, conducting polymer and their composite electrode materials for supercapacitor — a review, J. Energy Storage 52 (PC) (2022) 104937, https://doi.org/10.1016/j.est.2022.104937.
[12] L. Kong, C. Zhang, J. Wang, W. Qiao, L. Ling, D. Long, Free-standing T-Nb2O5/graphene composite papers with ultrahigh gravimetric/volumetric capacitance for Li-ion intercalation pseudocapacitor, ACS Nano 9 (11) (2015) 11200–11208, https://doi.org/10.1021/acsnano.5b04737.
[13] J. Zhu, D. Yang, Z. Yin, Q. Yan, H. Zhang, Graphene and graphene-based materials for energy storage applications, Small 10 (17) (2014) 3480–3498, https://doi.org/10.1002/smll.201303202.
[14] Q.H. Wang, K. Kalantar-Zadeh, A. Kis, J.N. Coleman, M.S. Strano, Electronics and optoelectronics of two-dimensional transition metal dichalcogenides, Nat. Nanotechnol. 7 (11) (2012) 699–712, https://doi.org/10.1038/nnano.2012.193.
[15] X. Zhang, X.F. Qiao, W. Shi, J. Bin Wu, D.S. Jiang, P.H. Tan, Phonon and Raman scattering of two-dimensional transition metal dichalcogenides from monolayer, multilayer to bulk material, Chem. Soc. Rev. 44 (9) (2015) 2757–2785, https://doi.org/10.1039/c4cs00282b.
[16] C. Ataca, H. Şahin, S. Ciraci, Stable, single-layer MX 2 transition-metal oxides and dichalcogenides in a honeycomb-like structure, J. Phys. Chem. C 116 (16) (2012) 8983–8999, https://doi.org/10.1021/jp212558p.
[17] D. Voiry, A. Mohite, M. Chhowalla, Phase engineering of transition metal dichalcogenides, Chem. Soc. Rev. 44 (9) (2015) 2702–2712, https://doi.org/10.1039/c5cs00151j.
[18] X. Yu, S. Yun, J.S. Yeon, P. Bhattacharya, L. Wang, S.W. Lee, X. Hu, H.S. Park, Emergent pseudocapacitance of 2D nanomaterials, Adv. Energy Mater. 8 (13) (2018) 1–33, https://doi.org/10.1002/aenm.201702930.
[19] Z. Wang, R. Li, C. Su, K.P. Loh, Intercalated phases of transition metal dichalcogenides, SmartMat 1 (1) (2020) 1–27, https://doi.org/10.1002/smm2.1013.
[20] L. Pi, L. Li, K. Liu, Q. Zhang, H. Li, T. Zhai, Recent progress on 2D noble-transition-metal dichalcogenides, Adv. Funct. Mater. 29 (51) (2019), https://doi.org/10.1002/adfm.201904932.
[21] R. Wang, Y. Yu, S. Zhou, H. Li, H. Wong, Z. Luo, L. Gan, T. Zhai, Strategies on phase control in transition metal dichalcogenides, Adv. Funct. Mater. 28 (47) (2018), https://doi.org/10.1002/adfm.201802473.
[22] J. Xu, J. Zhang, W. Zhang, C.S. Lee, Interlayer nanoarchitectonics of two-dimensional transition-metal dichalcogenides nanosheets for energy storage and conversion applications, Adv. Energy Mater. 7 (23) (2017) 1–30, https://doi.org/10.1002/aenm.201700571.
[23] Y. Jiao, A.M. Hafez, D. Cao, A. Mukhopadhyay, Y. Ma, H. Zhu, Metallic MoS2 for high performance energy storage and energy conversion, Small 14 (36) (2018) 1–20, https://doi.org/10.1002/smll.201800640.
[24] C. Gong, Y. Zhang, W. Chen, J. Chu, T. Lei, J. Pu, L. Dai, C. Wu, Y. Cheng, T. Zhai, L. Li, J. Xiong, Electronic and optoelectronic applications based on 2D novel anisotropic transition metal dichalcogenides, Adv. Sci. 4 (12) (2017), https://doi.org/10.1002/advs.201700231.
[25] S. Aftab, A.A. Al-Kahtani, M.Z. Iqbal, S. Hussain, G. Koyyada, Recent advances in 2D wearable flexible sensors, Adv Mater Technol 8 (14) (2023) 1–21, https://doi.org/10.1002/admt.202202168.

[26] S. Aftab, H.H. Hegazy, Emerging trends in 2D TMDs photodetectors and piezo-phototronic devices, Small 19 (18) (2023) 1–24, https://doi.org/10.1002/smll.202205778.

[27] E. Lee, Y.S. Yoon, D.J. Kim, Two-dimensional transition metal dichalcogenides and metal oxide hybrids for gas sensing, ACS Sens. 3 (10) (2018) 2045–2060, https://doi.org/10.1021/acssensors.8b01077.

[28] J. Ping, Z. Fan, M. Sindoro, Y. Ying, H. Zhang, Recent advances in sensing applications of two-dimensional transition metal dichalcogenide nanosheets and their composites, Adv. Funct. Mater. 27 (19) (2017) 1–18, https://doi.org/10.1002/adfm.201605817.

[29] K. Kanahashi, J. Pu, T. Takenobu, 2D materials for large-area flexible thermoelectric devices, Adv. Energy Mater. 10 (11) (2020) 1–23, https://doi.org/10.1002/aenm.201902842.

[30] S. Manzeli, D. Ovchinnikov, D. Pasquier, O.V. Yazyev, A. Kis, 2D transition metal dichalcogenides, Nat. Rev. Mater. 2 (2017), https://doi.org/10.1038/natrevmats.2017.33.

[31] X. Huang, J. Tang, B. Luo, R. Knibbe, T. Lin, H. Hu, M. Rana, Y. Hu, X. Zhu, Q. Gu, D. Wang, L. Wang, Sandwich-like ultrathin TiS2 nanosheets confined within N, S codoped porous carbon as an effective polysulfide promoter in lithium-sulfur batteries, Adv. Energy Mater. 9 (32) (2019) 1–9, https://doi.org/10.1002/aenm.201901872.

[32] T. Liu, X. Zhang, M. Xia, H. Yu, N. Peng, C. Jiang, M. Shui, Y. Xie, T.F. Yi, J. Shu, Functional cation defects engineering in TiS2 for high-stability anode, Nano Energy 67 (November 2019) (2020) 104295, https://doi.org/10.1016/j.nanoen.2019.104295.

[33] M. Mazaherifar, M. Elahi, M. Pourfath, Anisotropic electronic and plasmonic properties of 2H-TiS2, J. Phys. D Appl. Phys. 54 (19) (2021), https://doi.org/10.1088/1361-6463/abcfe6.

[34] Y. Zhou, J. Wan, Q. Li, L. Chen, J. Zhou, H. Wang, D. He, X. Li, Y. Yang, H. Huang, Chemical welding on semimetallic TiS2 nanosheets for high-performance flexible n-type thermoelectric films, ACS Appl. Mater. Interfaces 9 (49) (2017) 42430–42437, https://doi.org/10.1021/acsami.7b15026.

[35] J. Zha, Z. Yuan, Z. Zhou, Y. Li, J. Zhao, Z. Zeng, L. Zhen, H. Tai, C. Tan, H. Zhang, Self-assembly of 2D nanosheets into 1D nanostructures for sensing NO 2, Small Struct 2 (9) (2021) 2100067, https://doi.org/10.1002/sstr.202100067.

[36] N. Sakhuja, R.K. Jha, R. Chaurasiya, A. Dixit, N. Bhat, 1T-Phase titanium disulfide nanosheets for sensing H2S and O2, ACS Appl. Nano Mater. 3 (4) (2020) 3382–3394, https://doi.org/10.1021/acsanm.0c00127.

[37] Y. Zhang, B. Zheng, C. Zhu, X. Zhang, C. Tan, H. Li, B. Chen, J. Yang, J. Chen, Y. Huang, L. Wang, H. Zhang, Single-layer transition metal dichalcogenide nanosheet-based nanosensors for rapid, sensitive, and multiplexed detection of DNA, Adv. Mater. 27 (5) (2015) 935–939, https://doi.org/10.1002/adma.201404568.

[38] D. Yeniterzi, S.C. Cevher, S. Kandur Baglicakoglu, A.D. Ucar, M.B. Durukan, T. Hacıefendioğlu, E. Yıldırım, A. Cirpan, H.E. Unalan, S. Soylemez, Two-dimensional TiS2 nanosheet and conjugated polymer nanoparticles- based composites for sensing applications, ACS Langmuir (2024), https://doi.org/10.1016/j.sc.2020.00372. *Preprint*.

[39] A.J. Huckaba, S. Gharibzadeh, M. Ralaiarisoa, C. Roldán-Carmona, N. Mohammadian, G. Grancini, Y. Lee, P. Amsalem, E.J. Plichta, N. Koch, A. Moshaii, M.K. Nazeeruddin, Low-cost TiS 2 as hole-transport material for perovskite solar cells, Small Methods 1 (10) (2017) 1700250, https://doi.org/10.1002/smtd.201700250.

[40] M. Lickleder, G. Cha, R. Hahn, P. Schmuki, Ordered nanotubular titanium disulfide (TiS 2) structures: synthesis and use as counter electrodes in dye sensitized solar cells (DSSCs), J. Electrochem. Soc. 166 (5) (2019) H3009–H3013, https://doi.org/10.1149/2.0031905jes.

[41] L. Wang, Y. Tang, Y. Li, C. Liu, N. Wei, W. Zeng, D. Liang, Multifunctional integrated interdigital microsupercapacitors and self-powered iontronic tactile pressure sensor for wearable electronics, ACS Appl. Mater. Interfaces 14 (41) (2022) 47136–47147, https://doi.org/10.1021/acsami.2c15117.

[42] C. Wan, X. Gu, F. Dang, T. Itoh, Y. Wang, H. Sasaki, M. Kondo, K. Koga, K. Yabuki, G.J. Snyder, R. Yang, K. Koumoto, Flexible N-type thermoelectric materials by organic intercalation of layered transition metal dichalcogenide TiS 2, Nat. Mater. 14 (6) (2015) 622–627, https://doi.org/10.1038/nmat4251.

[43] S.J. Varma, J. Kumar, Y. Liu, K. Layne, J. Wu, C. Liang, Y. Nakanishi, A. Aliyan, W. Yang, P.M. Ajayan, J. Thomas, 2D TiS2 layers: a superior nonlinear optical limiting material, Adv. Opt. Mater. 5 (24) (2017) 1–9, https://doi.org/10.1002/adom.201700713.

[44] M.S. Whittingham, Lithium titanium disulfide cathodes, Nat. Energy 6 (2) (2021) 214, https://doi.org/10.1038/s41560-020-00765-7.

[45] K. Sun, M. Fu, Z. Xie, D. Su, H. Zhong, J. Bai, E. Dooryhee, H. Gan, Improvement of Li-S battery electrochemical performance with 2D TiS2 additive, Electrochim. Acta 292 (2018) 779–788, https://doi.org/10.1016/j.electacta.2018.09.191.

[46] S.H. Chung, L. Luo, A. Manthiram, TiS2-Polysulfide hybrid cathode with high sulfur loading and low electrolyte consumption for lithium-sulfur batteries, ACS Energy Lett. 3 (3) (2018) 568–573, https://doi.org/10.1021/acsenergylett.7b01321.

[47] S.H. Chung, A. Manthiram, A Li2S-TiS2-Electrolyte composite for stable Li2S-based lithium–sulfur batteries, Adv. Energy Mater. 9 (30) (2019) 1–9, https://doi.org/10.1002/aenm.201901397.

[48] Z. Hu, Z. Tai, Q. Liu, S.W. Wang, H. Jin, S. Wang, W. Lai, M. Chen, L. Li, L. Chen, Z. Tao, S.L. Chou, Ultrathin 2D TiS 2 nanosheets for high capacity and long-life sodium ion batteries, Adv. Energy Mater. 9 (8) (2019) 1–8, https://doi.org/10.1002/aenm.201803210.

[49] G. Alvarez Ferrero, G. Åvall, K.A. Mazzio, Y. Son, K. Janßen, S. Risse, P. Adelhelm, Co-intercalation batteries (CoIBs): role of TiS2 as electrode for storing solvated Na ions, Adv. Energy Mater. 12 (47) (2022), https://doi.org/10.1002/aenm.202202377.

[50] J. Park, S.J. Kim, K. Lim, J. Cho, K. Kang, Reconfiguring sodium intercalation process of TiS2Electrode for sodium-ion batteries by a partial solvent cointercalation, ACS Energy Lett. 7 (10) (2022) 3718–3726, https://doi.org/10.1021/acsenergylett.2c01838.

[51] D.Y. Oh, Y.E. Choi, D.H. Kim, Y.G. Lee, B.S. Kim, J. Park, H. Sohn, Y.S. Jung, All-solid-state lithium-ion batteries with TiS2 nanosheets and sulphide solid electrolytes, J Mater Chem A Mater 4 (26) (2016) 10329–10335, https://doi.org/10.1039/c6ta01628f.

[52] R. Zhang, X. Yang, S. Xu, D. Xu, F. Du, A kinetics study on intercalation pseudocapacitance of layered TiS2 in K-ion batteries, Phys. Chem. Chem. Phys. 21 (47) (2019) 25940–25944, https://doi.org/10.1039/c9cp04254g.

[53] X. Sun, P. Bonnick, L.F. Nazar, Layered TiS2 positive electrode for Mg batteries, ACS Energy Lett. 1 (1) (2016) 297–301, https://doi.org/10.1021/acsenergylett.6b00145.

[54] E. Long, S. O'Brien, E.A. Lewis, E. Prestat, C. Downing, C.S. Cucinotta, S. Sanvito, S.J. Haigh, V. Nicolosi, An in situ and ex situ TEM study into the oxidation of titanium (IV) sulphide, NPJ 2D Mater Appl 1 (1) (2017) 1–8, https://doi.org/10.1038/s41699-017-0024-4.

[55] C.S. Cucinotta, K. Dolui, H. Pettersson, Q.M. Ramasse, E. Long, S.E. O'Brian, V. Nicolosi, S. Sanvito, Electronic properties and chemical reactivity of TiS2 nanoflakes, J. Phys. Chem. C 119 (27) (2015) 15707–15715, https://doi.org/10.1021/acs.jpcc.5b03212.

[56] V. Vega-Mayoral, R. Tian, A.G. Kelly, A. Griffin, A. Harvey, M. Borrelli, K. Nisi, C. Backes, J.N. Coleman, Solvent exfoliation stabilizes TiS2 nanosheets against oxidation, facilitating lithium storage applications, Nanoscale 11 (13) (2019) 6206–6216, https://doi.org/10.1039/c8nr09446b.

[57] S. Takayanagi, Y. Sugahara, R. Guégan, Enhanced electrochemical performances of heterostructures based on the colloidal association of graphene oxide and titanium disulfide nanosheets, Langmuir (2024), https://doi.org/10.1021/acs.langmuir.4c02515.

[58] M.A. Rahman, M.A. Haque, M.A.A. Shaikh, C.K. Roy, A.H. Reaz, M.T.A. Shawon, P. K. Baksi, S. Yasmin, M.H. Kabir, S.H. Won, T.W. Kim, M.M. Rahman, Titanium sulfide thin film coated titanium foil for high-performance symmetric supercapacitor, J. Energy Storage 99 (PA) (2024) 113205, https://doi.org/10.1016/j.est.2024.113205.

[59] E.D. Grayfer, M.N. Kozlova, V.E. Fedorov, Colloidal 2D nanosheets of MoS2 and other transition metal dichalcogenides through liquid-phase exfoliation, Adv. Colloid Interface Sci. 245 (April) (2017) 40–61, https://doi.org/10.1016/j.cis.2017.04.014.

[60] E.D. Grayfer, M.N. Kozlova, V.E. Fedorov, Colloidal 2D nanosheets of MoS2 and other transition metal dichalcogenides through liquid-phase exfoliation, Adv. Colloid Interface Sci. 245 (April) (2017) 40–61, https://doi.org/10.1016/j.cis.2017.04.014.

[61] F. Ghani, A.A. Haidry, A. Raza, Q. Fatima, Y. Weng, M. Sajjad, M.D. Albaqami, S. Mohammad, Anisotropic CO adsorption and enhanced O2 activation on defective TiS2 monolayer: a dft study, Mater. Today Commun. 40 (February) (2024) 109680, https://doi.org/10.1016/j.mtcomm.2024.109680.

[62] P.C. Sherrell, K. Sharda, C. Grotta, J. Ranalli, M.S. Sokolikova, F.M. Pesci, P. Palczynski, V.L. Bemmer, C. Mattevi, Thickness-dependent characterization of chemically exfoliated TiS2 nanosheets, ACS Omega 3 (8) (2018) 8655–8662, https://doi.org/10.1021/acsomega.8b00766.

[63] P. Huang, L. Yuan, K. Zhang, Q. Chen, Y. Zhou, B. Song, Y. Li, Room-temperature and aqueous solution-processed two-dimensional TiS2 as an electron transport layer for highly efficient and stable planar n-i-p perovskite solar cells, ACS Appl. Mater. Interfaces 10 (17) (2018) 14796–14802, https://doi.org/10.1021/acsami.8b03225.

[64] T.Y. Ko, D. Kim, S.J. Kim, H. Kim, A.S. Nissimagoudar, S.C. Lee, X. Lin, P. T. Cummings, S. Doo, S. Park, T. Hassan, T. Oh, A. Chae, J. Lee, Y. Gogotsi, I. In, C. M. Koo, Universal ligands for dispersion of two-dimensional MXene in organic solvents, ACS Nano (2022), https://doi.org/10.1021/acsnano.2c08209.

[65] C. Lin, X. Zhu, J. Feng, C. Wu, S. Hu, J. Peng, Y. Guo, L. Peng, J. Zhao, J. Huang, J. Yang, Y. Xie, Hydrogen-incorporated TiS2 ultrathin nanosheets with ultrahigh conductivity for stamp-transferrable electrodes, J. Am. Chem. Soc. 135 (13) (2013) 5144–5151, https://doi.org/10.1021/ja400041f.

[66] A.L. Let, D.E. Mainwaring, C. Rix, P. Murugaraj, Thio sol-gel synthesis of titanium disulfide thin films and powders using titanium alkoxide precursors, J. Non-Cryst. Solids 354 (15–16) (2008) 1801–1807, https://doi.org/10.1016/j.jnoncrysol.2007.09.005.

[67] S.M. Andonova, G. Senturk, E. Kayhan, E. Ozensoy, Nature of the Ti-Ba interactions on the BaO/TiO2/Al2O3 NOx storage system, J. Phys. Chem. C 113 (2009) 11014–11026.

[68] H. Hemmatpour, O. De Luca, D. Crestani, M.C.A. Stuart, A. Lasorsa, P.C.A. van der Wel, K. Loos, T. Giousis, V. Haddadi-Asl, P. Rudolf, New insights in polydopamine formation via surface adsorption, Nat. Commun. 14 (1) (2023) 1–12, https://doi.org/10.1038/s41467-023-36303-8.

[69] H.S. Varol, T. Herberger, M. Kirsch, J. Mikolei, L. Veith, V. Kannan-Sampathkumar, R.D. Brand, C.V. Synatschke, T. Weil, A. Andrieu-Brunsen, Electropolymerization of polydopamine at electrode-supported insulating mesoporous films, Chem. Mater. 35 (21) (2023) 9192–9207, https://doi.org/10.1021/acs.chemmater.3c01890.

[70] H. Martinez, C. Auriel, D. Gonbeau, M. Loudet, G. Pfister-Guillouzo, Studies of 1T TiS 2 by STM, AFM and XPS: the mechanism of hydrolysis in air, Appl. Surf. Sci. 93 (3) (1996) 231–235, https://doi.org/10.1016/0169-4332(95)00339-8.
[71] J.C. Dupin, D. Gonbeau, I. Martin-Litas, P. Vinatier, A. Levasseur, Amorphous oxysulfide thin films MOySz (M = W, Mo, Ti) XPS characterization: structural and electronic pecularities, Appl. Surf. Sci. 173 (1–2) (2001) 140–150, https://doi.org/10.1016/S0169-4332(00)00893-X.
[72] W.J. Lee, Y.M. Sung, Synthesis of anatase nanosheets with exposed (001) facets via chemical vapor deposition, Cryst. Growth Des. 12 (11) (2012) 5792–5795, https://doi.org/10.1021/cg301317j.
[73] J.A. Rodriguez, S. Chaturvedi, M. Kuhn, J. Hrbek, Reaction of H 2 S and S 2 with metal/oxide surfaces: band-gap size and chemical reactivity the adsorption and dissociation of H 2 S and S 2 on a series of oxide, J. Phys. Chem. B 102 (98) (1998) 5511–5519.
[74] E. Pameté, L. Köps, F.A. Kreth, S. Pohlmann, A. Varzi, T. Brousse, A. Balducci, V. Presser, The many deaths of supercapacitors: degradation, aging, and performance fading, Adv. Energy Mater. (2023) 2301008, https://doi.org/10.1002/aenm.202301008.
[75] F. Ursi, S. Virga, G. Garc, N. Masciocchi, A. Martorana, F. Giannici, Long-Term Stability of TiS 2 – Alkylamine Hybrid Materials, 2022.
[76] M. Acerce, D. Voiry, M. Chhowalla, Metallic 1T phase MoS2 nanosheets as supercapacitor electrode materials, Nat. Nanotechnol. 10 (4) (2015) 313–318, https://doi.org/10.1038/nnano.2015.40.
[77] E. Yabaş, E. Biçer, M.B. Durukan, D. Keskin, H.E. Unalan, Double-decker lutetium and europium phthalocyanine composites with reduced graphene oxide as supercapacitor electrode materials, J. Organomet. Chem. 980–981 (2022) 122509, https://doi.org/10.1016/j.jorganchem.2022.122509.
[78] Y. Liao, H. Wang, M. Zhu, A. Thomas, Efficient supercapacitor energy storage using conjugated microporous polymer networks synthesized from buchwald–hartwig coupling, Adv. Mater. 30 (12) (2018) 1–10, https://doi.org/10.1002/adma.201705710.
[79] V. Vivier, M.E. Orazem, Impedance analysis of electrochemical systems, Chem Rev 122 (12) (2022) 11131–11168, https://doi.org/10.1021/acs.chemrev.1c00876.
[80] S.K. Babu, J.J.D. Raj, T. Vijayakumar, B. Gunasekaran, Experimental and DFT studies on spinel NiMn2O4 flower derived from bimetallic MOF as an efficient electrode for next-generation supercapacitor, Colloids Surf. A Physicochem. Eng. Asp. 655 (July) (2022) 130244, https://doi.org/10.1016/j.colsurfa.2022.130244.
[81] S. Fleischmann, J.B. Mitchell, R. Wang, C. Zhan, D.E. Jiang, V. Presser, V. Augustyn, Pseudocapacitance: from fundamental understanding to high power energy storage materials, Chem Rev 120 (14) (2020) 6738–6782, https://doi.org/10.1021/acs.chemrev.0c00170.
[82] C.R. Chen, H. Qin, H.P. Cong, S.H. Yu, A highly stretchable and real-time healable supercapacitor, Adv. Mater. 31 (19) (2019) 1–10, https://doi.org/10.1002/adma.201900573.
[83] K. Jayaramulu, D.P. Dubal, B. Nagar, V. Ranc, O. Tomanec, M. Petr, K.K.R. Datta, R. Zboril, P. Gómez-Romero, R.A. Fischer, Ultrathin hierarchical porous carbon nanosheets for high-performance supercapacitors and redox electrolyte energy storage, Adv. Mater. 30 (15) (2018) 1–9, https://doi.org/10.1002/adma.201705789.
[84] Z. Yan, Z. Gao, Z. Zhang, C. Dai, W. Wei, P.K. Shen, Graphene nanosphere as advanced electrode material to promote high performance symmetrical supercapacitor, Small 17 (18) (2021) 1–12, https://doi.org/10.1002/smll.202007915.
[85] J.S. Ko, C.H. Lai, J.W. Long, D.R. Rolison, B. Dunn, J. Nelson Weker, Differentiating double-layer, psuedocapacitance, and battery-like mechanisms by analyzing impedance measurements in three dimensions, ACS Appl. Mater. Interfaces 12 (12) (2020) 14071–14078, https://doi.org/10.1021/acsami.0c02020.
[86] S. Fleischmann, H. Shao, P.L. Taberna, P. Rozier, P. Simon, Electrochemically induced deformation determines the rate of lithium intercalation in bulk TiS2, ACS Energy Lett. 6 (12) (2021) 4173–4178, https://doi.org/10.1021/acsenergylett.1c01934.
[87] T.S. Mathis, N. Kurra, X. Wang, D. Pinto, P. Simon, Y. Gogotsi, Energy storage data reporting in perspective—guidelines for interpreting the performance of electrochemical energy storage systems, Adv. Energy Mater. 9 (39) (2019) 1–13, https://doi.org/10.1002/aenm.201902007.
[88] M.A. Bissett, I.A. Kinloch, R.A.W. Dryfe, Characterization of MoS2-graphene composites for high-performance coin cell supercapacitors, ACS Appl. Mater. Interfaces 7 (31) (2015) 17388–17398, https://doi.org/10.1021/acsami.5b04672.
[89] Y.A. Kumar, C.J. Raorane, H.H. Hegazy, T. Ramachandran, S.C. Kim, M. Moniruzzaman, 2D MXene-based supercapacitors: a promising path towards high-performance energy storage, J. Energy Storage 72 (PB) (2023) 108433, https://doi.org/10.1016/j.est.2023.108433.
[90] C. Tian, Effects of structural factors of hydrated TiO2 on rutile TiO2 pigment preparation via short sulfate process, Sci. Rep. 10 (1) (2020), https://doi.org/10.1038/s41598-020-64976-4.
[91] X. Ren, P. Geng, Q. Jiang, Q. Ren, D.K. Macharia, N. Yu, Z. Chen, Synthesis of degradable titanium disulfide nanoplates for photothermal ablation of tumors, Mater Today Adv 14 (2022) 100241, https://doi.org/10.1016/j.mtadv.2022.100241.
[92] H. Martinez, C. Auriel, D. Gonbeau, M. Loudet, G. Pfister-Guillouzo, Surface analysis of two misfit layer compounds - (PbS) 1.18 (TiS 2) and (PbS) 1.18 (TiS 2) 2 - by scanning probe microscopies (AFM and STM) and X-ray photoelectron spectroscopy (XPS), Appl. Surf. Sci. 125 (3–4) (1998) 259–272, https://doi.org/10.1016/S0169-4332(97)00503-5.
[93] X. Zang, C. Shen, E. Kao, R. Warren, R. Zhang, K.S. Teh, J. Zhong, M. Wei, B. Li, Y. Chu, M. Sanghadasa, A. Schwartzberg, L. Lin, Titanium disulfide coated carbon nanotube hybrid electrodes enable high energy density symmetric pseudocapacitors, Adv. Mater. 30 (5) (2018) 1–8, https://doi.org/10.1002/adma.201704754.
[94] J. Tang, X. Huang, T. Lin, T. Qiu, H. Huang, X. Zhu, Q. Gu, B. Luo, L. Wang, MXene derived TiS2 nanosheets for high-rate and long-life sodium-ion capacitors, Energy Storage Mater. 26 (November 2019) (2020) 550–559, https://doi.org/10.1016/j.ensm.2019.11.028.
[95] A. Chaturvedi, P. Hu, V. Aravindan, C. Kloc, S. Madhavi, Unveiling two-dimensional TiS2 as an insertion host for the construction of high energy Li-ion capacitors, J Mater Chem A Mater 5 (19) (2017) 9177–9181, https://doi.org/10.1039/c7ta01594a.
[96] A. Chaturvedi, P. Hu, Y. Long, C. Kloc, S. Madhavi, V. Aravindan, High power Na-ion capacitor with TiS2 as insertion host, Scr Mater 161 (2019) 54–57, https://doi.org/10.1016/j.scriptamat.2018.10.016.
[97] L. Zhang, F. Kühling, A.-M. Mattsson, L. Knijff, X. Hou, G. Ek, T. Dufils, F. Holm Gjørup, I. Kantor, C. Zhang, W.R. Brant, K. Edström, E.J. Berg, Reversible hydration enabling high-rate aqueous Li-ion batteries, ACS Energy Lett. (2024) 959–966, https://doi.org/10.1021/acsenergylett.4c00224.